Stability of superconducting $Nd_{0.8}Sr_{0.2}NiO_2$ thin films

Xiang Ding[1†], Shengchun Shen[2†], Huaqian Leng[1], Minghui Xu[1], Yan Zhao[1], Junrui Zhao[1], Xuelei Sui[3], Xiaoqiang Wu[4], Haiyan Xiao[1], Xiaotao Zu[1], Bing Huang[3], Huiqian Luo[5,6], Pu Yu[2], and Liang Qiao[1*]

[1] *School of Physics, University of Electronic Science and Technology of China, Chengdu 610054, China;*
[2] *Department of Physics, Tsinghua University, Beijing 100084, China;*
[3] *Beijing Computational Science Research Center, Beijing 100193, China;*
[4] *School of Mechanical Engineering, Chengdu University, Chengdu 610106, China;*
[5] *Beijing National Laboratory for Condensed Matter Physics, Institute of Physics, Chinese Academy of Sciences, Beijing 100190, China;*
[6] *Songshan Lake Materials Laboratory, Dongguan 523808, China*

The discovery of superconducting states in the nickelate thin film with infinite-layer structure has paved a new way for studying unconventional superconductivity. So far, research in this field is still very limited due to difficulties in sample preparation. Here we report the successful preparation of the superconducting state of $Nd_{0.8}Sr_{0.2}NiO_2$ thin film (T_c = 8.0-11.1 K) and study the stability of such films in the ambient environment, water, and under electrochemical conditions. Our work demonstrates that the superconducting state of $Nd_{0.8}Sr_{0.2}NiO_2$ is remarkably stable, which can last for at least 47-day continuous exposure to air at 20°C and 35% relative humidity. We also show that the superconductivity disappears after being immersed in de-ionized water at room temperature for 5 h. Surprisingly, it can also survive under ionic liquid gating conditions with an applied voltage of about 4 V, which is even more stable than conventional perovskite complex oxides.

nickelate superconductor, stability, ionic liquid gating

PACS number(s): 74.78.-w, 74.70.-b, 74.25.Fy

1 Introduction

The discovery of superconductivity in epitaxial nickelate film by Li et al. [1] has recently attracted significant attention due to the delicate position of nickel in the periodic table, i.e., between copper and iron. Therefore, superconducting nickelates are expected to establish a connection between the copper and iron-based high-temperature superconductors (HTS) and provide a clue to understanding the pairing me-

chanism in HTS [1-3]. Although nickelates show similarities with cuprates, e.g., infinite-layer structure, $3d^9$ configuration, and even similar phase diagram [4,5], many fundamental issues of them remain unraveled. Compared with cuprate and pnictide HTS [6-10], it shows much lower onset superconducting transition temperature (T_c) [11], weaker insulating characters outside the superconducting dome [4], Mott-Hubbard-type band structure [12,13], unclear magnetic structure/interactions, and absence of superconductivity in bulk materials [14-16]. Unlike cuprates and other oxide superconductors that can be easily synthesized through conventional ceramic or film synthesis techniques, the

superconducting nickelate film seems to be rather vulnerable due to its narrow growth window and unclear topotactical reduction mechanism.

The removal of apical oxygen in perovskite nickelates is crucial to achieving two-dimensional NiO_2 planes based on superconducting infinite-layer nickelates. The pioneering work of using CaH_2 to reduce the perovskite structure to obtain an infinite-layer structure was reported as early as 1983 [17]. However, superconductivity in nickelate is still in its infancy stage. Due to our limited knowledge of the secondary phase formation and underlying mechanism of the reduction process, effective synthesis control of infinite-layer nickelate superconductor appears to be extremely difficult. Since the first discovery of nickel-based superconductor in 2019, nearly two hundred related articles have been published. Most of these articles are theoretical and experimental studies that only account for a small part [1,4,5,11-14,18-28]. Particularly, only a few research groups worldwide can reproduce the superconducting nickelate epitaxial films [1,5,19,23,26,29].

Recently, significant progress has been demonstrated in experimental studies. Li et al. [4] and Zeng et al. [5] have independently reported Sr substitution dependent superconducting phase diagram. They identified a superconducting dome with optimized Sr concentration between 12% and 25%, which is in analogy to the well-known superconducting dome for cuprates. Goodge et al. [13] employed state-of-the-art electron microscopy with electron energy-loss spectroscopy to probe the Mott-Hubbard character of $Nd_{1-x}Sr_xNiO_2$. They observed emergent hybridization reminiscent of the Zhang-Rice singlet, providing direct evidence for the multiband electronic structure of the superconducting infinite-layer nickelates. Charge density waves have been discovered in undoped and less Sr doped $NdNiO_2$ and $LaNiO_2$ films [30-32]. However, there are some controversies on the magnetic ground states of superconducting nickelates. Zeng et al. [33] used a superconducting quantum interference device to measure the magnetic properties of superconducting and determined a perfect diamagnetism. However, Lu et al. [27] studied pristine and doped $NdNiO_2$ using resonant inelastic X-ray scattering (RIXS) to obtain interesting low-energy magnon excitations with antiferromagnetic correlations. Some preliminary nuclear magnetic resonance (NMR) has recently been conducted on the infinite-layer nickelates. For instance, Zhao et al. [34] found a paramagnetic ground state in $LaNiO_2$ (^{139}La NMR). Additionally, Cui et al. [18] observed a short-range antiferromagnetic ordering by proton-enriched $Nd_{0.85}Sr_{0.15}NiO_2$ (^{1}H NMR). These NMR samples are powder samples without superconductivity, and the results are yet to be fully understood.

Despite important breakthroughs, many basic properties of this new superconducting system are still unclear, such as

efficient preparation, environmental stability, and carrier concentration controllability of these infinite-layer nickelates. In particular, the stability of superconductivity in infinite nickelates is crucial for future applications. To this end, we report the successful synthesis of $Nd_{0.8}Sr_{0.2}NiO_2$ thin films and study their environmental stability. Epitaxial $Nd_{0.8}Sr_{0.2}NiO_2$ are prepared using pulsed laser deposition (PLD) and successive topochemical reduction method, showing the highest superconducting transition temperature (T_c) ~11.1 K. The superconductivity is found to be rather stable, even exposed in the air at 20°C and 35% relative humidity (RH) for at least 47 d. However, the sample soaked in de-ionized water at room temperature lost its superconductivity in 5 h. Additionally, the superconducting nickelate film shows a high energy barrier for the evolution of hydrogen and oxygen ions, evidenced by *in situ* ionic liquid gating (ILG) [35-38], suggesting stability against strong electrochemical conditions.

2 Experimental methods

The $Nd_{0.8}Sr_{0.2}NiO_2$ films with the infinite-layer structure are prepared by topochemical reduction of perovskite $Nd_{0.8}Sr_{0.2}NiO_3$ without a capping layer. $Nd_{0.8}Sr_{0.2}NiO_3$ films (thickness about 14.5-16 nm) are deposited on TiO_2-terminated STO (001) substrates by 248-nm KrF laser [39,40]. During deposition, the substrate temperature is controlled at 620°C with an oxygen pressure of 200 mTorr (1 Torr = 1.33322 $\times 10^2$ Pa). A laser fluence of 1 J/cm^2 was used to ablate the target, and the size of the laser spot is about 3 mm^2. After deposition, the samples were cooled down in the same oxygen pressure at the rate of 10°C/min. The as-grown samples were cut into four pieces and sealed in the quartz tube with 0.1 g CaH_2 to acquire the infinite-layer nickelate phase. The pressure of the tube is about 0.3 mTorr [41]. After that, the tube was heated for about 300°C in the tube furnace and held for 2 h before naturally cooling down, with the ramp rate of 10°C/min. The crystal structure of films is characterized using a Bruker D8 Discover diffractometer in diffraction and reflectance mode. A hybrid monochromator, consisting of four-bounce double-crystal Ge (220) and a Cu X-ray mirror, was placed in the incident beam path to generate monochromated Cu Kα_1 X rays (λ = 1.54 Å) with a beam divergence of 12 arcsec and angular precision of 0.0001°. Temperature-dependent resistivity and Hall effect were measured using the four-probe method and van der Pauw geometry in a cryogen-free magnet system (Cryogenic Ltd.) and physical properties measurement system (Quantum Design Inc.) with magnetic fields of about 9 T and a temperature of 1.6 K. Electrical contact of Al wires was bond on deposited Au pads on the film surface by ultrasonic wire bonder. For *in situ* electrical transport in ILG, the sample was

placed in a quartz bowl covered entirely with ionic liquid, and a slice of Pt was used as the gate electrode. The gate voltage (V_G) was changed at room temperature with a dwell time of 10 min for each cycle.

3   Results and discussion

Figure 1(a) shows X-ray diffraction (XRD) 2θ-ω scans of as-grown $Nd_{0.8}Sr_{0.2}NiO_3$ and reduced $Nd_{0.8}Sr_{0.2}NiO_2$. After reduction, the film peaks shift from low to high 2θ values, revealing the successful removal of apical oxygen atoms in perovskite $Nd_{0.8}Sr_{0.2}NiO_3$ and realization of infinite-layer $Nd_{0.8}Sr_{0.2}NiO_2$. The determined c axis lattice constant shrinks from 3.76 to 3.36 Å (nearly by 11% reduction), consistent with previous work [42]. Figure 1(b) shows the experimental X-ray reflectivity (XRR) data of films (before and after CaH$_2$ reduction) and corresponding fitting curves (based on the LEPTOS 7.10 software [43]). Kiessig fringes are clear in the XRR curves for perovskite and infinite-layer structures, providing another approach for determining the thickness of the epitaxial thin film. The fitted thickness before and after the reduction are 14.7 and 13.8 nm, respectively. Therefore, the film thickness shrinks only by 6%, which is less than the nominal 11% shrinkage value of the

lattice constant according to the diffraction peak position. The discrepancy reflects there must be defect formation, which is associated with the Ruddlesden-Popper (RP)-type faults, as reported in various superconducting infinite-layer nickelates systems through transmission electron microscopy [11,24,44].

Figure 1(c) and (d) show the in-plane resistivity $\rho(T)$ of $Nd_{0.8}Sr_{0.2}NiO_2$ film at different magnetic fields with in-plane (IP, $H\perp c$) and out-of-plane (OOP, $H//c$) directions. Under the zero-field condition, the pristine film shows obvious onset (offset) T_c at 11.1 K (8.2 K). Here, onset (offset) is defined as temperatures at which the resistivity is 90% (10%) of the resistivity value at 20 K. In the high-temperature region ($T >$ 50 K), $\rho(T)$ shows nearly linear behaviors in the normal states, as shown by the dashed line in the inset of Figure 1(c). This is also consistent with previous understanding of metallic nickelate and its unconventional nature with possible non-Fermi liquid (NFL) state. In principle, the in-plane resistivity $\rho(T)$ can be fitted by a power law: $\rho(T) = \alpha T^n + \rho_0$, where ρ_0 is the residual resistivity, and α is a measure of the strength of electron-phonon scattering. For a Fermi liquid system, $n = 2$, $n < 2$ usually means an NFL behavior. In this case, $n = 1$ indicates possible quantum criticality in this system. Such linear $\rho(T)$ in the normal state is a hallmark of abnormal behaviors in cuprates. In our superconducting
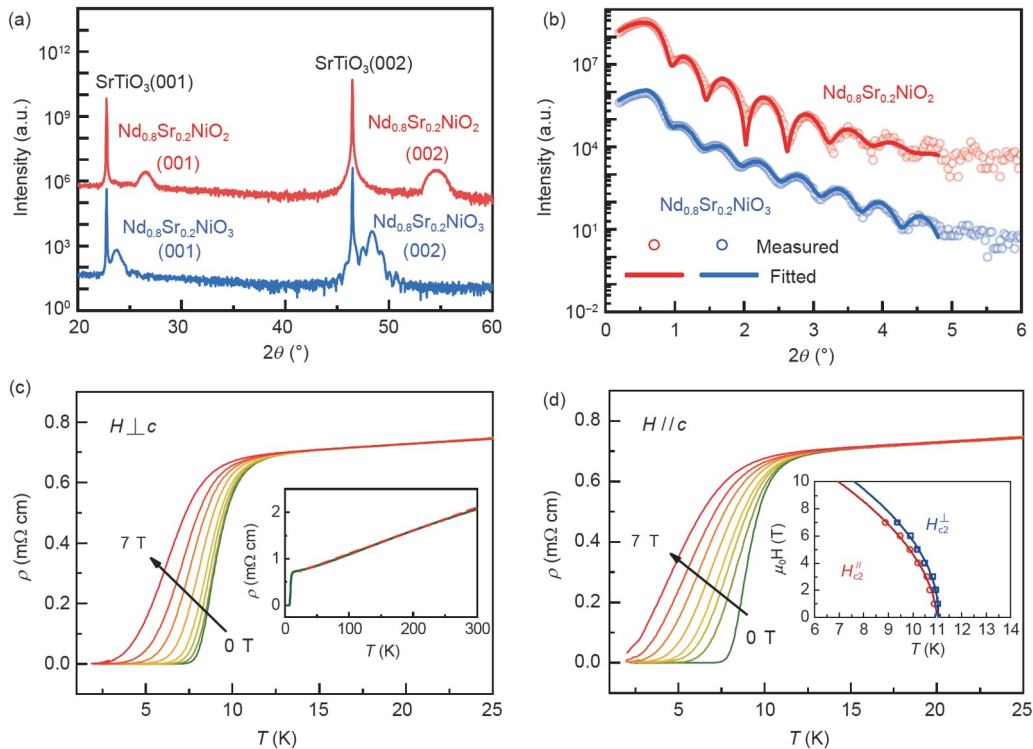
Figure 1   (Color online) (a) XRD 2θ-ω scans of typical $Nd_{0.8}Sr_{0.2}NiO_3$ and $Nd_{0.8}Sr_{0.2}NiO_2$ films with a thickness of about 15 nm. (b) Measured with fitted XRR of as-grown $Nd_{0.8}Sr_{0.2}NiO_3$ and reduced $Nd_{0.8}Sr_{0.2}NiO_2$. $\rho(T)$ of $Nd_{0.8}Sr_{0.2}NiO_2$ film with magnetic field perpendicular (c) and parallel (d) to the c axis. The insert of (c) shows the resistivity variation at all temperatures, and the dashed red line is the linear fitting of the normal-state resistivity curve. The inset of (d) shows H_{c2}-T phase diagrams for magnetic fields along and perpendicular to the c axis. The upper critical field is obtained using the 90% resistivity criterion.

films, we obtain that the α, ρ_0, and residual resistance ratio (RRR = ρ(300 K)/ρ_0) are sample sensitive. For example, α varies from 1.2 to 5.8 $\mu\Omega$ cm/K; ρ_0 locates between 0.18 and 0.8 mΩ cm; the RRR value varies from 3.2 to 4.4. These results are consistent with the reported values in previous studies [1,19,20]. The changes in these parameters reflect the variation of film crystal quality. This may originate because the competing phases of RP faults and perovskite during epitaxial growth show comparative formation energies; thus, they always coexist. The critical role of the defects on carrier transport for superconducting nickelates deserves further systematically investigation. Meanwhile, transport measurement under an external magnetic field shows a similar broadening tendency of suppressed superconductivity in the IP and OOP magnetic fields. The H_{c2}-T phase diagrams in Figure 1(d) indicate largely isotropic behavior in different field directions, revealing that the superconductivity in nickelates has three-dimensional (3D) characteristics. These observations are generally consistent with the reported transport measurements [20,24].

After confirming the basic physical properties of the superconducting film, we started studying the stability of the film. To the best of our knowledge, many copper-oxide superconductors degrade rapidly in the presence of air, which contains oxygen, carbon dioxide, and moisture [45]. Among

published experiments, most superconducting samples are stored in a vacuum chamber or even in a glove box under a nitrogen atmosphere to avoid contact with oxygen and moisture in the air [19,20]. However, the stability of infinite nickelate in air condition is still unclear. Therefore, it is essential to evaluate the stability of infinite-layer nickelates in this condition. To answer this question, a superconducting sample without a capping layer was prepared and exposed in the air at ambient conditions (20°C, 35% RH) to measure its $\rho(T)$ curve and temperature-dependent normal-state Hall coefficient (R_H) for several days of about 47 d. As shown in Figure 2(a), the superconductivity hardly changes, except for a very slight increase in normal-state resistivity over time. We obtained that the increase in resistivity is not linear but has a power relationship with exposure time (t), i.e., $\rho(t) \propto t^{0.5}$. As a proxy for this law, resistivity versus exposure time at 150 K (ρ(150 K)) is shown in the inset of Figure 2(a). Figure 2(b) shows the details in the superconducting transition regime. Although the resistance increases monotonically with time, the change in T_c is very slight (see Figure 2(b) inset).

Figure 2(c) shows the temperature-dependent R_H corresponding to Figure 2(a) for films exposed to air for about 47 d. The linear behavior of R_{xy} up to 7 T at different temperatures enables us to efficiently extract R_H (Figure 2(d)). It
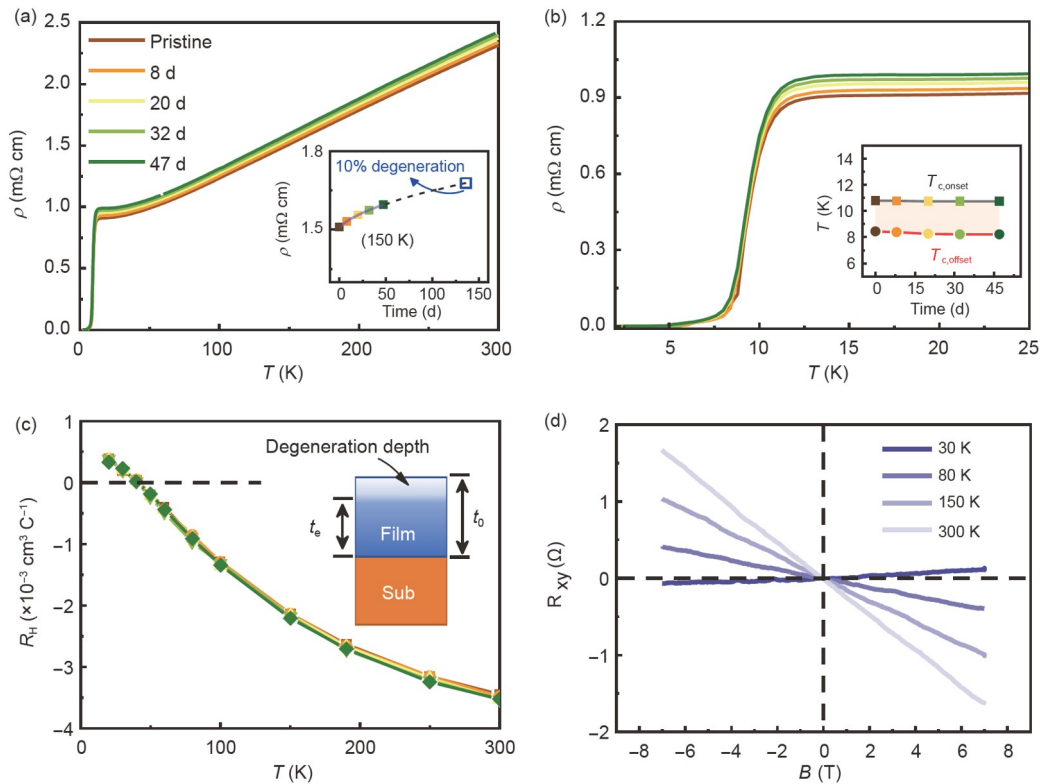
Figure 2   (Color online) (a), (b) $\rho(T)$ of a superconducting Nd$_{0.8}$Sr$_{0.2}$NiO$_2$ film continuously exposed to air for weeks. The inset of (a) shows the ρ(150 K) vs. exposure time (solid squares) and the fitting curve. The blue hollow-square indicates the film with predicted 10% degeneration. The inset of (b) shows superconducting transition temperatures. (c) Normal-state Hall coefficient $R_H(T)$ corresponding to (a). The inset illustrates the surface degeneration model. (d) Linear behavior of Hall resistances R_{xy} in superconducting film.

is obvious that R_H has a strong temperature dependence. At room temperature, the R_H has a negative sign and large magnitude, which is attributed to negatively-charged electrons with low concentration. As the temperature decreases, the carrier concentration gradually increases and finally transitions to hole-type carriers (< 40 K). The above analysis of Hall data is based on simple carrier density ($n = 1/eR_H$, where e is the electron charge) estimation. Generally, $Nd_{0.8}Sr_{0.2}NiO_2$ is expected to be a hole-type superconductor due to divalent Sr-doping on the rare-earth position; thus, the Hall coefficient should be positive. However, *n*-type behavior can also be observed due to the complex band structure and self-doping effect from the Nd element (detailed explanation can be found in the following discussion). As a result, the positive and negative Hall coefficients are determined through Hall measurement. Although the exact physical origin of both types of carriers is unclear, our data are consistent with previous reports [4,5]. It is evidenced that the Hall coefficient of the sample in an air environment is very stable, except for the Hall coefficient at room temperature deviates a little to pristine curve. As the temperature decreases, the deviation gradually decreases. Therefore, our data suggest that superconducting nickelates are stable in conventional ambient conditions (dry air), and a glove box is unnecessary for sample storage.

Then, we move from air to water. It is well-known that different cuprate superconductors exhibit significant variation in their water reactivity. For example, the famous $YBa_2Cu_3O_7$ is highly sensitive to water and vapor [46]. In this respect, moisture in the air may be the culprit, increasing resistivity. Therefore, it is meaningful to study the water stability of the superconductivity in nickelates. For this purpose, another superconducting film was soaked in deionized water at 20°C. With increasing immersion time, the film diffraction peaks gradually weaken, broaden and finally disappear (Figure 3(a)), revealing that water at room temperature strongly degrades the structure of $Nd_{0.8}Sr_{0.2}NiO_2$. Here, five hours is a critical time. Before that, the diffraction peak intensity did not change significantly. Meanwhile, after that, the intensity started decaying.

Correspondingly, this critical time is also reflected in the transport measurements. Figure 3(b) summarizes the resistivity evolution of film soaked in water. Superconductivity still exists within 2 h of immersion. However, the sample lost its zero-resistance character when soaked for 5 h. The resistivity is saturated at a finite value (0.5 mΩ cm) at low temperatures, while the superconducting transition still exists. Once the strength of the diffraction peaks is weakened (corresponding to 8 h), an insulating state emerges. Further prolonging the immersion time, i.e., more than 10 h, would result in complete insulation ($\rho > 700$ Ω cm at room temperature). Figure 3(c) shows a zoom-in view of Figure 3(b), focusing on the details of the superconducting transition regime. Within 2 h, as the immersion time increases, the increase in resistivity is similar to the sample in air, except that the resistivity changes more drastically. The inset of Figure 3(c) shows the rapid change in T_c, suggesting an obvious broadening effect in the superconducting transition.
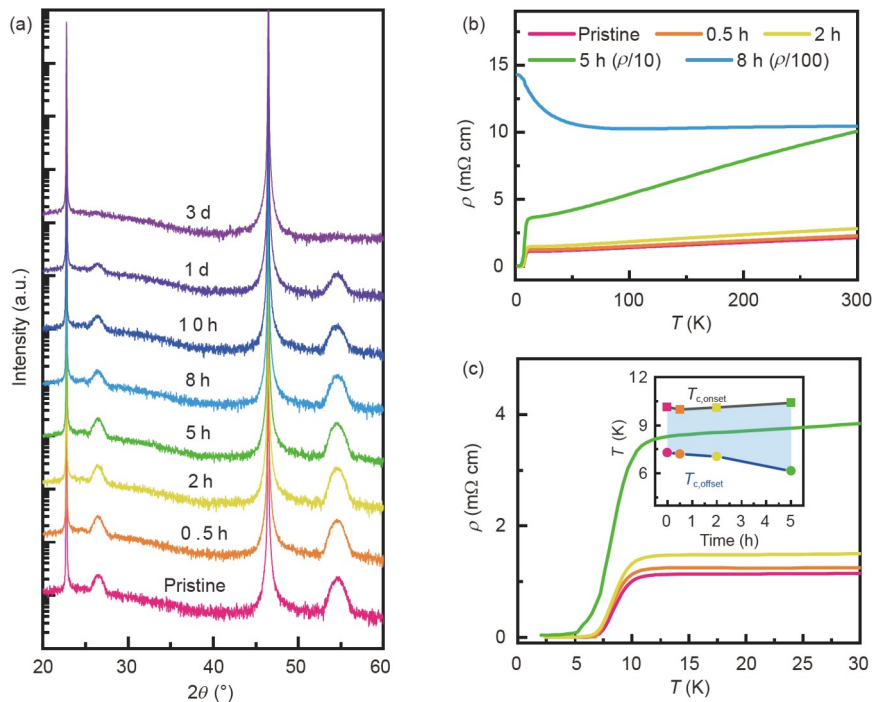
Figure 3 (Color online) (a) XRD 2θ-ω scans evolution of a superconducting sample immersed in water. The curves are vertically offset for clarity. (b) $\rho(T)$ curve vs. immersion time. (c) A zoom-in view of (b). The inset of (c) shows superconducting transition temperature under different immersion times.

Combined with the aging test in air and water, it is reasonable that moisture is the main cause of the degradation of the sample in the air. Additionally, degradation is a gradual process that starts from the reaction of water/moisture and superconducting film at the surface. The oxygen and carbon dioxide in the air are secondary factors. Water seems to be the natural nemesis of high-T_c superconductivity, and nickel-based superconductivity is no exception.

A simple surface degeneration model is proposed to explain the above phenomena based on two assumptions. The first assumption is that water/moisture could gradually decompose the sample from the top (surface) to the bottom. As illustrated in the inset of Figure 2(c), the actual effective thickness (t_e) of the superconducting film would gradually become thinner than the original thickness (t_0) due to the surface reaction with moisture. Since the film thickness was considered the default value (t_0) during testing, meaning $t_e \leq t_0$, we assume that $t_e = t_0$ in the pristine measurement. In the subsequent exposure process, the surface of the sample gradually degrades, resulting in a gradual decrease in t_e. The second assumption is that the resistivity in t_e part is the same as that of pristine. This assumption is reasonable because the degenerated layer on the surface is insulating, which would not contribute to the conduction. Additionally, the trivial change in the superconducting transition supports this hypothesis (inset of Figure 2(b)).

According to the resistivity relationship: $R = G \cdot \rho \cdot t_e^{-1}$, where G is the geometric factor depending on the electrode position. The electrode position has not changed in the experiment; therefore, G is a constant in all measurements. Then, the resistance R is only proportional to t_e^{-1}, indicating that a decrease in t_e leads to an increase in R. Since we used t_0 instead of t_e by default in the measurement, resistivity is calculated as $\rho = G \cdot R \cdot t_0$. As a result, the resistivity ρ is overestimated than the actual $G \cdot R \cdot t_e$. The reduction in the effective thickness t_e leads to an increase in R. Since the change in the thickness is ignored, dividing the resistance R by the original thickness t_0 directly would result in an apparent increase in resistivity.

In turn, based on this model, we can calculate the effective thickness t_e, which is the actual superconducting layer. In the pristine case, $R_{pristine} = G \cdot \rho \cdot t_0^{-1}$, while for degraded same film, $R_{degraded} = G \cdot \rho \cdot t_e^{-1}$. Therefore, $t_e/t_0 = R_{pristine}/R_{degraded} = \rho_{pristine}/\rho_{degraded}$. Our calculation shows that after 47 d in the ambient dry air, the t_e/t_0 ratio is 0.95, indicating a 5% depth degeneration on the surface. It has been pointed out that the resistivity change versus exposure time has a relationship like $\rho(t) \propto t^{0.5}$. Therefore, based on the above model, if we take the resistivity change at 150 K as an example, we obtain that it takes a total of 136 d to reach 10% degeneration of $\rho_{pristine}$, i.e., another 89 d after the experimentally determined 47 d. The predicted 10% degeneration depth is shown in the inset of Figure 2(a). Therefore, to delay surface damage, a dry environment is preferred. Meanwhile, the effective thickness estimations for the sample soaked in water are 93.5% (0.5 h), 75% (2 h), and 2.5% (5 h). The first two values seem reasonable, whereas the effective thickness for 5 h is too thin to be metallic. We have to point out that the degradation of the film in water may not be as uniform as in air due to the strong interaction with water. The superconducting transition is obviously broadened (inset of Figure 3(c)) in several hours due to the strong reaction between water and thin film. This indicates that the strong interaction could influence the electrical properties of effective layers and make the degeneration depth deviate from the surface degeneration model.

For the past few decades, ILG has shown great power in regulating carrier density (close to 8×10^{14} cm^{-2}) in various materials [47-49]. It also has the potential to induce structural phase transition, i.e., the insertion of oxygen ions (negative voltage) or hydrogen ions (positive voltage) in the pristine material, such as in epitaxial SrCoO$_{2.5}$ thin films [35]. As a similar complex oxide whose apical oxygens are removed by chemical reduction, infinite-layer structured Nd$_{0.8}$Sr$_{0.2}$NiO$_2$ might be prone to be re-oxidized back to perovskite Nd$_{0.8}$Sr$_{0.2}$NiO$_3$ or at least, Nd$_{0.8}$Sr$_{0.2}$NiO$_{2+\delta}$. Once this happens, the recovered apical oxygen atom will suppress the superconductivity in nickelates film and changes its temperature-dependent resistivity curve.

With this motivation, we further explore the stability of the infinite-layer Nd$_{0.8}$Sr$_{0.2}$NiO$_2$ superconducting thin film under stronger perturbation conditions, such as direct electrochemical gating, to see if electrical properties can be effectively tuned. As shown in Figure 4, under the influence of ILG, the changes in T_c and R_H are slight in a wide voltage window between −1 and 4 V. Since the upper limit of carrier modulation of ILG is about 10^{15} cm^{-2}, the observed insensitivity of the Hall coefficient to an applied electric field indicates that the intrinsic carrier density of nickelates is above this limit. In such a high carrier density, an order of about 10^{15} cm^{-2} control level provided by ILG is insufficient in tuning the carrier concentration in the film, leading to an unchanged Hall coefficient.

In addition to the above explanation, the complex nature of infinite nickelates band structure might contribute to the observed stability of R_H under gating. In contrast to the well-established single orbital model developed for cuprates [50], superconducting nickelates demonstrate a unique and more complex band structure due to the simultaneous involvement of Nd 5d$_{xy}$ electron pocked by self-doping and lifted Ni 3d$_{x^2-y^2}$ orbital near the Fermi level [2,51]. Thus, the carrier density cannot be directly derived from the Hall coefficient measurement. Although the 3D rare-earth 5d orbital hybridizes with quasi-2D Ni 3d orbitals, it is still unclear what effect the 5d band may have on the strongly correlated Ni 3d
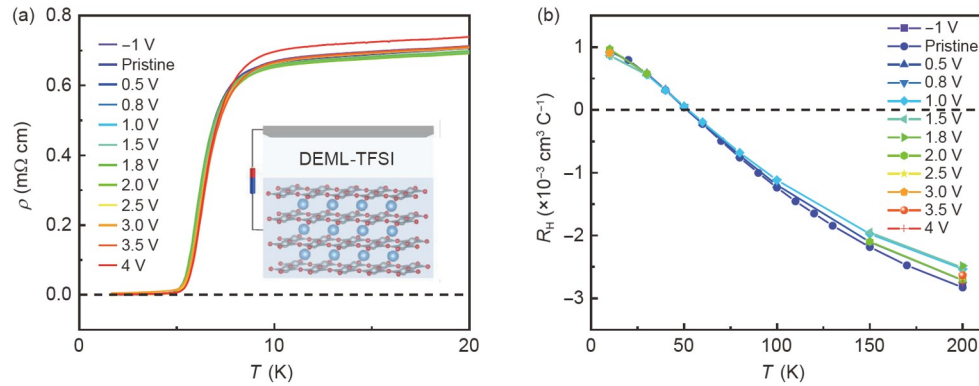
Figure 4 (Color online) (a) Temperature-dependence resistivity at multiple gate voltages in ionic-liquid gated $Nd_{0.8}Sr_{0.2}NiO_2$ film. The inset picture shows the schematic of the ionic-liquid-gated device. (b) Temperature-dependent Hall coefficient at multiple gate voltages in ionic-liquid gated $Nd_{0.8}Sr_{0.2}NiO_2$ film.

band [52]. These facts increase the complexity of the data analysis. We infer that this multiband character leads to carrier extraction failure and needs more exploration.

Figure 4(a) and (b) also show that the aforementioned structural phase transition does not appear in the current infinite-layer $Nd_{0.8}Sr_{0.2}NiO_2$ system. Based on previous reports, oxygenation and protonation could occur in cuprates and iron pnictides [38,53]. In these experiments, 60-nm $Pr_2CuO_{4\pm\delta}$ thin film and bulk iron pnictides (the 11 and 122 structures) show phase transition in the voltage window between −1 and 4 V. However, it is remarkably surprising that no obvious transport change can be observed in infinite nickelates in such a wide voltage interval. The unchanged structural and electrical properties of the superconducting nickelate film under ILG suggest a relatively high energy barrier for hydrogen or oxygen ion evolution, indicating that the superconducting nickelate film maintains robust against the electrochemical environment.

4 Conclusion

In this study, we prepared superconducting nickelate samples using PLD. XRD demonstrates the transition of $Nd_{0.8}Sr_{0.2}$-NiO_3 to $Nd_{0.8}Sr_{0.2}NiO_2$, and the temperature-dependent resistivity reveals the onset T_c about 8.0-11.1 K. We obtain that the superconductivity is quite stable with only a slight increase in resistivity by exposing the superconducting sample in the air (20°C, 35% RH) for 47 d. However, the superconductivity degrades quickly when a sample is immersed in water. We also developed a simple surface degeneration model to explain the increase in resistivity. These results show that the superconductivity in nickelates is stable in dry air for a long time, and it is sensitive to moisture and water. Therefore, a low-humidity environment is preferable for their application. Further experiments demonstrate that ILG has little influence on the superconductivity and transport properties of the $Nd_{0.8}Sr_{0.2}NiO_2$ film. This also indicates that

nickelate superconductor is very robust even in a harsh electrochemical environment.

1   D. Li, K. Lee, B. Y. Wang, M. Osada, S. Crossley, H. R. Lee, Y. Cui, Y. Hikita, and H. Y. Hwang, Nature **572**, 624 (2019).

2   A. S. Botana, and M. R. Norman, Phys. Rev. X **10**, 011024 (2020).

3   D. F. Li, Sci. Sin.-Phys. Mech. Astron. **51**, 047405 (2021).

4   D. Li, B. Y. Wang, K. Lee, S. P. Harvey, M. Osada, B. H. Goodge, L. F. Kourkoutis, and H. Y. Hwang, Phys. Rev. Lett. **125**, 027001 (2020).

5   S. Zeng, C. S. Tang, X. Yin, C. Li, M. Li, Z. Huang, J. Hu, W. Liu, G. J. Omar, H. Jani, Z. S. Lim, K. Han, D. Wan, P. Yang, S. J. Pennycook, A. T. S. Wee, and A. Ariando, Phys. Rev. Lett. **125**, 147003 (2020).

6   X. Chen, P. Dai, D. Feng, T. Xiang, and F. C. Zhang, Natl. Sci. Rev. **1**, 371 (2014).

7   P. A. Lee, N. Nagaosa, and X. G. Wen, Rev. Mod. Phys. **78**, 17 (2006).

8   Y. Fei, Y. Zheng, K. L. Bu, W. H. Zhang, Y. Ding, X. J. Zhou, and Y. Yin, Sci. China-Phys. Mech. Astron. **63**, 227411 (2019).

9   T. Wang, J. N. Chu, J. X. Feng, L. L. Wang, X. G. Xu, W. Li, H. H. Wen, X. S. Liu, and G. Mu, Sci. China-Phys. Mech. Astron. **63**, 297412 (2020).

10   X. Yu, Z. Wei, Z. Zhao, T. Xie, C. Liu, G. He, Q. Chen, L. Shan, H. Luo, Q. Huan, J. Yuan, and K. Jin, Sci. China-Phys. Mech. Astron. **64**, 127411 (2021).

11   M. Osada, B. Y. Wang, B. H. Goodge, S. P. Harvey, K. Lee, D. Li, L. F. Kourkoutis, and H. Y. Hwang, Adv. Mater. **33**, 2104083 (2021).

12   M. Hepting, D. Li, C. J. Jia, H. Lu, E. Paris, Y. Tseng, X. Feng, M. Osada, E. Been, Y. Hikita, Y. D. Chuang, Z. Hussain, K. J. Zhou, A. Nag, M. Garcia-Fernandez, M. Rossi, H. Y. Huang, D. J. Huang, Z. X. Shen, T. Schmitt, H. Y. Hwang, B. Moritz, J. Zaanen, T. P. Devereaux, and W. S. Lee, Nat. Mater. **19**, 381 (2020).

13   B. H. Goodge, D. Li, K. Lee, M. Osada, B. Y. Wang, G. A. Sawatzky, H. Y. Hwang, and L. F. Kourkoutis, Proc. Natl. Acad. Sci. USA **118**, e2007683118 (2021).

14   Q. Li, C. He, J. Si, X. Zhu, Y. Zhang, and H. H. Wen, Commun. Mater. **1**, 16 (2020).

15   Y. Ji, J. Liu, L. Li, and Z. Liao, J. Appl. Phys. **130**, 060901 (2021).

16   Q. Li, C. P. He, X. Y. Zhu, J. Si, X. W. Fan, and H. H. Wen, Sci. China-Phys. Mech. Astron. **64**, 227411 (2020).

17   M. Crespin, P. Levitz, and L. Gatineau, J. Chem. Soc. Faraday Trans. 2 **79**, 1181 (1983).

18   Y. Cui, C. Li, Q. Li, X. Zhu, Z. Hu, Y. Yang, J. Zhang, R. Yu, H. H. Wen, and W. Yu, Chin. Phys. Lett. **38**, 067401 (2021).

19   Q. Gao, Y. Zhao, X. J. Zhou, and Z. Zhu, Chin. Phys. Lett. **38**, 077401 (2021).

20 Y. Xiang, Q. Li, Y. Li, H. Yang, Y. Nie, and H. H. Wen, Chin. Phys. Lett. **38**, 047401 (2021).

21 Y. Li, W. Sun, J. Yang, X. Cai, W. Guo, Z. Gu, Y. Zhu, and Y. Nie, Front. Phys. **9**, 443 (2021).

22 M. Osada, B. Y. Wang, B. H. Goodge, K. Lee, H. Yoon, K. Sakuma, D. Li, M. Miura, L. F. Kourkoutis, and H. Y. Hwang, Nano Lett. **20**, 5735 (2020).

23 Q. Gu, Y. Li, S. Wan, H. Li, W. Guo, H. Yang, Q. Li, X. Zhu, X. Pan, Y. Nie, and H. H. Wen, Nat. Commun. **11**, 6027 (2020).

24 B. Y. Wang, D. Li, B. H. Goodge, K. Lee, M. Osada, S. P. Harvey, L. F. Kourkoutis, M. R. Beasley, and H. Y. Hwang, Nat. Phys. **17**, 473 (2021).

25 B. X. Wang, H. Zheng, E. Krivyakina, O. Chmaissem, P. P. Lopes, J. W. Lynn, L. C. Gallington, Y. Ren, S. Rosenkranz, J. F. Mitchell, and D. Phelan, Phys. Rev. Mater. **4**, 084409 (2020).

26 X. R. Zhou, Z. X. Feng, P. X. Qin, H. Yan, X. N. Wang, P. Nie, H. J. Wu, X. Zhang, H. Y. Chen, Z. A. Meng, Z. W. Zhu, and Z. Q. Liu, Rare Met. **40**, 2847 (2021).

27 H. Lu, M. Rossi, A. Nag, M. Osada, D. F. Li, K. Lee, B. Y. Wang, M. Garcia-Fernandez, S. Agrestini, Z. X. Shen, E. M. Been, B. Moritz, T. P. Devereaux, J. Zaanen, H. Y. Hwang, K. J. Zhou, and W. S. Lee, Science **373**, 213 (2021).

28 Q. Gu, and H. H. Wen, Innovation **3**, 100202 (2022).

29 N. N. Wang, M. W. Yang, K. Y. Chen, Z. Yang, H. Zhang, Z. H. Zhu, Y. Uwatoko, X. L. Dong, K. J. Jin, J. P. Sun, and J.-G. Cheng, arXiv: 2109.12811.

30 G. Krieger, L. Martinelli, S. Zeng, L. E. Chow, K. Kummer, R. Arpaia, M. M. Sala, N. B. Brookes, A. Ariando, and N. Viart, arXiv: 2112.03341.

31 M. Rossi, M. Osada, J. Choi, S. Agrestini, D. Jost, Y. Lee, H. Lu, B. Y. Wang, K. Lee, A. Nag, Y.-D. Chuang, C.-T. Kuo, S.-J. Lee, B. Moritz, T. P. Devereaux, Z.-X. Shen, J.-S. Lee, K.-J. Zhou, H. Y. Hwang, and W.-S. Lee, arXiv: 2112.02484.

32 C. C. Tam, J. Choi, X. Ding, S. Agrestini, A. Nag, B. Huang, H. Luo, M. García-Fernández, L. Qiao, and K.-J. Zhou, arXiv: 2112.04440.

33 S. W. Zeng, X. M. Yin, C. J. Li, C. S. Tang, K. Han, Z. Huang, Y. Cao, L. E. Chow, D. Y. Wan, Z. T. Zhang, Z. S. Lim, C. Z. Diao, P. Yang, A. T. S. Wee, S. J. Pennycook, and A. Ariando, arXiv: 2104.14195.

34 D. Zhao, Y. B. Zhou, Y. Fu, L. Wang, X. F. Zhou, H. Cheng, J. Li, D. W. Song, S. J. Li, B. L. Kang, L. X. Zheng, L. P. Nie, Z. M. Wu, M. Shan, F. H. Yu, J. J. Ying, S. M. Wang, J. W. Mei, T. Wu, and X. H. Chen, Phys. Rev. Lett. **126**, 197001 (2021).

35 N. Lu, P. Zhang, Q. Zhang, R. Qiao, Q. He, H. B. Li, Y. Wang, J. Guo, D. Zhang, Z. Duan, Z. Li, M. Wang, S. Yang, M. Yan, E. Arenholz, S. Zhou, W. Yang, L. Gu, C. W. Nan, J. Wu, Y. Tokura, and P. Yu, Nature **546**, 124 (2017).

36 Z. Li, S. Shen, Z. Tian, K. Hwangbo, M. Wang, Y. Wang, F. M. Bartram, L. He, Y. Lyu, Y. Dong, G. Wan, H. Li, N. Lu, J. Zang, H. Zhou, E. Arenholz, Q. He, L. Yang, W. Luo, and P. Yu, Nat. Commun. **11**, 184 (2020).

37 S. Shen, Z. Li, Z. Tian, W. Luo, S. Okamoto, and P. Yu, Phys. Rev. X **11**, 021018 (2021).

38 Y. Cui, G. Zhang, H. Li, H. Lin, X. Zhu, H. H. Wen, G. Wang, J. Sun, M. Ma, Y. Li, D. Gong, T. Xie, Y. Gu, S. Li, H. Luo, P. Yu, and W. Yu, Sci. Bull. **63**, 11 (2018).

39 X. Ding, B. Yang, H. Leng, J. H. Jang, J. Zhao, C. Zhang, S. Zhang, G. Cao, J. Zhang, R. Mishra, J. Yi, D. Qi, Z. Gai, X. Zu, S. Li, B. Huang, A. Borisevich, and L. Qiao, Adv. Funct. Mater. **31**, 2106466 (2021).

40 L. Qiao, T. C. Droubay, T. Varga, M. E. Bowden, V. Shutthanandan, Z. Zhu, T. C. Kaspar, and S. A. Chambers, Phys. Rev. B **83**, 085408 (2011).

41 S. Chen, J. Zhao, Q. Jin, S. Lin, S. Chen, H. Yao, J. Wang, Z. Fan, E. J. Guo, and H. Guo, Sci. China-Phys. Mech. Astron. **64**, 287711 (2021).

42 K. Lee, B. H. Goodge, D. Li, M. Osada, B. Y. Wang, Y. Cui, L. F. Kourkoutis, and H. Y. Hwang, APL Mater. **8**, 041107 (2020).

43 A. Ulyanenkov, Appl. Surf. Sci. **253**, 106 (2006).

44 M. Osada, B. Y. Wang, K. Lee, D. Li, and H. Y. Hwang, Phys. Rev. Mater. **4**, 121801 (2020).

45 J. P. Zhou, D. R. Riley, A. Manthiram, M. Arendt, M. Schmerling, and J. T. McDevitt, Appl. Phys. Lett. **63**, 548 (1993).

46 M. F. Yan, R. L. Barns, H. M. O'Bryan Jr., P. K. Gallagher, R. C. Sherwood, and S. Jin, Appl. Phys. Lett. **51**, 532 (1987).

47 J. T. Ye, S. Inoue, K. Kobayashi, Y. Kasahara, H. T. Yuan, H. Shimotani, and Y. Iwasa, Nat. Mater. **9**, 125 (2010).

48 K. Ueno, S. Nakamura, H. Shimotani, H. T. Yuan, N. Kimura, T. Nojima, H. Aoki, Y. Iwasa, and M. Kawasaki, Nat. Nanotech. **6**, 408 (2011).

49 X. Xi, H. Berger, L. Forró, J. Shan, and K. F. Mak, Phys. Rev. Lett. **117**, 106801 (2016).

50 G. M. Zhang, Y. Yang, and F. C. Zhang, Phys. Rev. B **101**, 020501 (2020).

51 H. Sakakibara, H. Usui, K. Suzuki, T. Kotani, H. Aoki, and K. Kuroki, Phys. Rev. Lett. **125**, 077003 (2020).

52 E. Been, W. S. Lee, H. Y. Hwang, Y. Cui, J. Zaanen, T. Devereaux, B. Moritz, and C. Jia, Phys. Rev. X **11**, 011050 (2021).

53 L. Ma, B. Lei, N. Wang, K. Yang, D. Liu, F. Meng, C. Shang, Z. Sun, J. Cui, C. Zhu, T. Wu, Z. Sun, L. Zou, and X. Chen, Sci. Bull. **64**, 653 (2019).